



# Sustainable fabrication of graphene oxide/manganese oxide composites for removing phenolic compounds by adsorption-oxidation process

Bei Zhang <sup>a, b</sup>, Ruiguang Zhao <sup>b</sup>, Dejun Sun <sup>b</sup>, Yujiang Li <sup>a, \*</sup>, Tao Wu <sup>b, \*\*</sup>

<sup>a</sup> Shandong Provincial Research Center for Water Pollution Control, School of Environmental Science and Engineering, Shandong University, Jinan, 250100, PR China

<sup>b</sup> Key Laboratory of Colloid and Interface Science of Education Ministry, Shandong University, Jinan, 250100, PR China

## ARTICLE INFO

### Article history:

Received 15 September 2018  
Received in revised form  
3 December 2018  
Accepted 7 January 2019  
Available online 8 January 2019

### Keywords:

Sustainable fabrication  
Acidic liquid waste  
Transformation pathways  
Ring cleavage products  
Regeneration

## ABSTRACT

To develop effective strategies for removing phenolic compounds, *in-situ* graphene oxide/manganese oxide (GO/MnO<sub>x</sub>, X = 2, 3/4) composites were fabricated via a sustainable method by synchronously utilizing manganese ions and acidic liquid waste during synthesis of GO. Comparatively, traditionally *ex-situ* GO/MnO<sub>2</sub> composites were synthesized to verify the difference between *in-situ* and *ex-situ* synthesis. Based on the schematic and mass flow analysis, *in-situ* synthesis exhibited better atom economy and less waste emission than *ex-situ* synthesis. Then, the results of batch experiments exhibited that GO/MnO<sub>x</sub> composites possessed higher removal efficiency and wider pH range for p-cresol (p-CR) and p-tert-butylphenol (p-TBP) than GO/MnO<sub>2</sub> composites. The maximum removal capacities of GO/MnO<sub>x</sub> composites were 107.68 mg/g for p-CR and 135.41 mg/g for p-TBP. And GO/MnO<sub>x</sub> composites could retain high removal efficiency for p-TBP (>90%) after five recycles. For *in-situ* GO/MnO<sub>x</sub> composites, GO sheets not only promoted the adsorption of phenolic compounds and by-products, but also enhanced the oxidation capacity of MnO<sub>x</sub> via an electron transfer interaction. Especially, the detection of ring cleavage products indicated further oxidation for p-TBP. Possessing an eco-friendly fabrication strategy and augmented adsorption-oxidation capability, *in-situ* GO/MnO<sub>x</sub> composites are expected to be applied in the removal of phenolic compounds.

© 2019 Elsevier Ltd. All rights reserved.

## 1. Introduction

Phenolic compounds have given rise to emerging concerns regarding human health and ecosystems due to their widespread use in the pharmaceutical, petroleum and petrochemical, pesticide, plastic, and paper industries (Danquah et al., 2018). Consisting of a hydroxyl group bonded directly to a benzene ring, phenolic compounds possess a stable conjugated system, leading to biological accumulation and poor biodegradability (Ou et al., 2018). Thus, an urgent need exists to develop an efficient method for removing phenolic compounds (Villar da Gama et al., 2018; Zhong et al., 2018).

Various methods, including chemical oxidation (Jiang et al., 2015), adsorption (Villar da Gama et al., 2018), and membrane separation (Zagklis and Paraskeva, 2015), have been reported to remove phenolic compounds. Among them, oxidation constitutes an effective and attractive method due to the potential to disrupt the structural stability of pollutants (Wang et al., 2015). Manganese oxides, ubiquitous in natural soil and synthetic materials, are traditional and cost-effective adsorbents and oxidants in wastewater treatment. Especially, manganese oxides are able to oxidize various aromatic Lewis bases, such as phenolic and aniline compounds (Grebel et al., 2016; Wang et al., 2018b). Previous studies demonstrated that phenolic compounds are susceptible to oxidation by manganese dioxide (MnO<sub>2</sub>) through sequential one electron-transfer reactions, forming a series of intermediate products (Abdullah et al., 2017; Remucal and Ginder-Vogel, 2014). However, the intermediate products, such as phenolic multimer and benzoquinones, would be released back into the aqueous solution. Meanwhile, during the oxidation of phenolic compounds, reductive

\* Corresponding author.

\*\* Corresponding author.

E-mail addresses: [zhangbeisdu@163.com](mailto:zhangbeisdu@163.com) (B. Zhang), [zrg3909@163.com](mailto:zrg3909@163.com) (R. Zhao), [djsun@sdu.edu.cn](mailto:djsun@sdu.edu.cn) (D. Sun), [yujiang@sdu.edu.cn](mailto:yujiang@sdu.edu.cn) (Y. Li), [wutao@sdu.edu.cn](mailto:wutao@sdu.edu.cn) (T. Wu).

dissolution of manganese oxides would occur (Grebel et al., 2016), leading to the release of manganese ions. The above by-products are undesirable in practical wastewater treatment processes. Thus, effective adsorption of the above by-products during or after the oxidation process is essential for avoiding secondary pollution.

In recent years, graphene oxide-based composites have attracted extensive attention as potential adsorbents based on the structural functionality and surface properties (Yan et al., 2014). Compared with traditional materials, the composite materials possess multifunction of different components, such as adsorption and oxidation properties (Awual, 2014, 2016, 2017). In addition, the synergistic effect of components in composites enhances the application prospect (Awual et al. 2015b, 2018). Especially, the reserved  $sp^2$ -hybridized carbon configurations in graphene oxide (GO) sheets possess strong adsorption ability to aromatic compounds with  $\pi$ - $\pi$  interactions (Jin et al., 2015). The oxygenated groups from GO sheets in aqueous solution can rapidly adsorb metal cation by electrostatic attraction. These excellent properties meet the precise need of effective adsorption for both phenolic compounds and by-products (aromatic intermediate products and  $Mn^{2+}$ ) during oxidation by manganese oxides. Thus, it is a significant and meaningful aim to develop graphene oxide/manganese oxide composites with efficient adsorption and oxidation capacity for removing phenolic compounds.

Up to date, various types of graphene oxide/manganese oxide composites have been reported and mainly applied as electrodes because of their remarkable electrochemical properties (Buke et al., 2018; Chen et al., 2010; Wan et al., 2018; Wang et al., 2018a; Ye et al., 2018). These excellent properties may also provide a new insight into the interaction with environmental pollutants (Deng et al., 2015; Xu et al., 2015b). However, the extant literature that relates to the removal of phenolic compounds directly by graphene oxide/manganese oxide composites remains limited. In particular, conventional preparation methods of graphene oxide/manganese oxide composites consume great amounts of chemicals and energy, and produce a large volume of highly acidic wastewater containing manganese ions (Duan et al., 2016; Jianguying et al., 2013; Qu et al., 2014; Rathour and Bhattacharya, 2018). Therefore, it is also significant to develop an eco-friendly method for preparing graphene oxide/manganese oxide composites.

Herein, this work presented a sustainable strategy to prepare *in-situ* graphene oxide/manganese oxide (GO/MnO<sub>X</sub>, X = 2, 3/4) composites. Based on the fabrication hypothesis and objective, manganese ions in acidic wastewater were served as Mn(II) source to synthesize MnO<sub>X</sub>, which directly anchored onto GO sheets to obtain GO/MnO<sub>X</sub> composites in the particularly acid condition. Thus, the proposed strategy provided an effective solution to recycle acidic wastewater and fabricate *in-situ* GO/MnO<sub>X</sub> composites. Further, traditionally *ex-situ* graphene oxide/manganese oxide (GO/MnO<sub>2</sub>) composites were synthesized to contrastively elucidate the removal difference for p-cresol (p-CR) and p-tert-butylphenol (p-TBP). Based on characterization and batch experiments, the unique synthesis process provided GO/MnO<sub>X</sub> composites with excellent physicochemical properties and enhanced adsorption-oxidation capacity for phenolic pollutants in comparison with GO/MnO<sub>2</sub> composites. Possessing the superiority of sustainable fabrication, convenient addition, and excellent adsorption-oxidation properties, GO/MnO<sub>X</sub> composites have great potential to be employed into practical environmental remediation.

## 2. Experimental

### 2.1. Chemicals and materials

Graphite powder (granularity  $\leq 30 \mu\text{m}$ ),  $\text{KMnO}_4$ ,  $\text{H}_2\text{SO}_4$  (98%),

$\text{MnSO}_4 \cdot \text{H}_2\text{O}$ , NaOH, ascorbic acid, and HCl were purchased from the Sinopharm Chemical Reagent Co., Ltd., with high chemical purity. p-cresol (p-CR) and p-tert-butylphenol (p-TBP) were purchased from the Shanghai Macklin Biochemical Co., Ltd., of analytical grade. Their physicochemical properties, such as molecular structure, molecular weight (MW), aqueous solubility ( $C_s$ ), and octanol-water partition coefficient ( $K_{OW}$ ) are listed in Table S1 in the Supporting Information. Deionized (DI) water was produced using an ultra-pure water purifier system, with a resistivity of  $18.2 \text{ M}\Omega \text{ cm}^{-1}$ . All chemicals and materials were used without further purification.

### 2.2. In-situ fabrication of GO/MnO<sub>X</sub> composites

Pristine graphene oxide (GO) and  $\text{MnO}_2$  were first synthesized as precursors (Hummers and Offeman, 1958; Zhang et al., 2018a). Detail of synthesis process was provided in the Supporting Information. As shown in Fig. 1a, *in-situ* GO/MnO<sub>X</sub> composites were fabricated as follows. Typically, during synthesis of GO, the graphite oxide/ $\text{MnSO}_4$  suspension was exfoliated by ultrasonication for 15 min. 250 mL of  $\text{KMnO}_4$  solution (0.05 M) was then directly dropped into this suspension with stirring at  $85^\circ\text{C}$  for 1 h. Then, the brown mixture was aged at  $60^\circ\text{C}$  for 6 h. GO/MnO<sub>X</sub> dispersion was then obtained by washing thoroughly with DI water. The final product, GO/MnO<sub>X</sub> powder, was obtained by a freeze-drying process.

### 2.3. Ex-situ preparation of GO/MnO<sub>2</sub> composites

In order to compare with *in-situ* GO/MnO<sub>X</sub> composites, *ex-situ* GO/MnO<sub>2</sub> composites were prepared as shown in Fig. 1b. Typically, GO powder was dispersed in 250 mL DI water by ultrasonication at 250 W for 5 min with a sonifier. A certain content of  $\text{MnSO}_4 \cdot \text{H}_2\text{O}$  solution was mixed with GO dispersion with stirring at  $85^\circ\text{C}$  for 1 h. Then, 250 mL of  $\text{KMnO}_4$  solution (0.05 M) was directly dropped into the suspension with stirring at  $85^\circ\text{C}$  for another 1 h. The following procedures to obtain GO/MnO<sub>2</sub> composites were the same as the above methods. To ensure an accurate comparative study, the theoretical content of GO and manganese oxide in GO/MnO<sub>X</sub> and GO/MnO<sub>2</sub> composites was equal by controlling the dosage of GO powder,  $\text{MnSO}_4 \cdot \text{H}_2\text{O}$ , and  $\text{KMnO}_4$ .

### 2.4. Characterization

The morphology of samples was characterized by field-emission scanning electron microscopy (FE-SEM, Hitachi SU8010, Japan), transmission electron microscope (TEM, JEM-1011, Japan; HRTEM, JEM-2100, Japan). Energy-dispersive X-ray spectroscopy (EDX, Hitachi SU8010, Japan) was utilized to investigate the composition of GO/MnO<sub>X</sub> and GO/MnO<sub>2</sub> composites. Surface area & porosity analyzer (ASAP, 2020 HD88, Micromeritics, U.S.A.) was used to analyze pore structure of samples. X-ray diffraction (XRD) spectra were measured to examine the structural properties of samples on a diffractometer (Rigaku D-Max 2200, Japan). Fourier transform infrared spectroscopy (FT-IR) spectra were obtained using a FT-IR spectrophotometer (JASCO, FT/IR-6300, Japan). To examine the elementary transformation of samples, X-ray photoelectron spectroscopy (XPS) analysis was carried out with an X-ray photoelectron spectrometer (Thermo ESCALAB 250XI, U.S.A.). Moreover, the zeta potential was determined by a zeta-potential analyzer (Zeta-PALS, Brookhaven, U.S.A.).

### 2.5. Batch experiment

Typical batch experiments were performed by dispersing samples (1.0 g/L) in solution of p-CR and p-TBP (50 mg/L) under

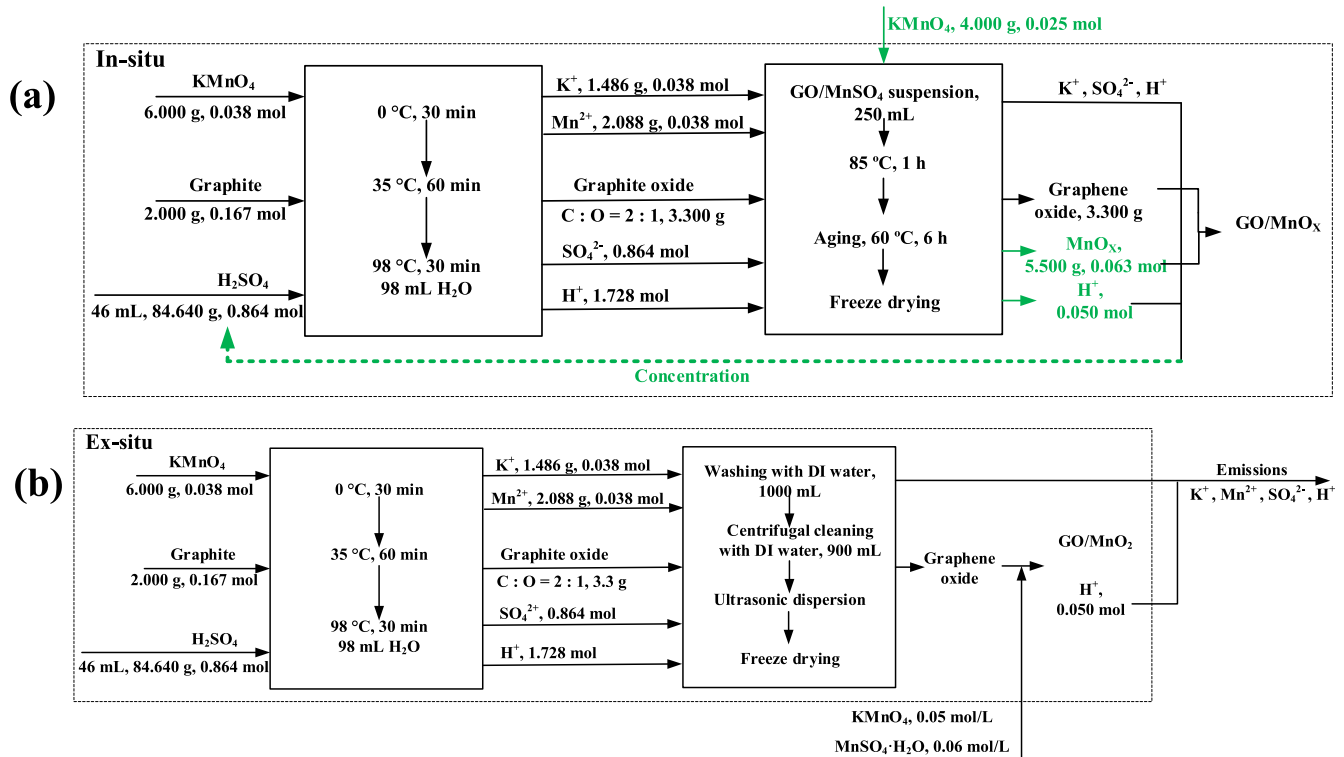


Fig. 1. Schematic of *in-situ* GO/MnO<sub>x</sub> composites (a) and *ex-situ* GO/MnO<sub>2</sub> composites (b) and mass flow analysis.

optimum condition (pH = 5, temperature = 25 °C). The samples (GO, MnO<sub>2</sub>, GO/MnO<sub>x</sub>, GO/MnO<sub>2</sub>) were selected to investigate the difference of removal efficiency for p-CR and p-TBP. In addition, to analyze the influence and optimize condition of pH for adsorption and oxidation pollutants, the initial solution pH (1–12) was adjusted by NaOH and HCl aqueous solution. Kinetic experiments at different temperatures (15 °C, 25 °C, and 35 °C) were also carried out to achieve optimum parameters with GO/MnO<sub>x</sub> and GO/MnO<sub>2</sub> composites for removal of p-CR and p-TBP. Ascorbic acid (0.01 M) was used to quenching reaction under optimum condition.

## 2.6. Regeneration experiment

To investigate the reusability of GO/MnO<sub>x</sub> and GO/MnO<sub>2</sub> composites, NaOH aqueous solution (0.1 M) was used as an eluent. The regenerated composites were then washed with DI water, and collected by centrifugal separation for the next cycle. The regeneration experiment was conducted under optimum parameters for five cycles.

## 2.7. Analytical methods

After the removal process, the supernatants of the mixture were separated by centrifugation (8000 rpm). The concentration of p-CR and p-TBP was measured using a UV/vis spectrometer (TU-1810 PC, China) and calculated by absorbance at 277 nm and 275 nm. The supernatants were filtrated by 0.22 μm membrane to measure total organic carbon (TOC) with an analyzer (TOC-V<sub>CPN</sub>, Shimadzu, Japan). Then, the organic contaminants from supernatants were analyzed by high performance liquid chromatography tandem-mass spectrometry (HPLC/MS-MS) with an Agilent 6460 system. The HPLC column used was an Agilent Zorbax SB-C18 column with the dimensions 2.1 mm × 50 mm and 1.8 μm pore size. Details of

the HPLC/MS-MS method parameters are provided in the Supporting Information. Furthermore, the concentration of Mn<sup>2+</sup> from supernatants during synthesis of samples and removal of pollutants was determined by formaldehyde oxime spectrophotometry (Kalembkiewicz et al., 2008). Specifically, the brown complex, generated from Mn and formaldehyde oxime under an alkaline condition, was measured using a UV/vis spectrometer (TU-1810 PC, China) at 450 nm.

The percentage of removal efficiency (R) for p-CR and p-TBP was calculated by the following equation (1):

$$R = (c_o - c_e) / c_o \times 100\% \quad (1)$$

The percentage of TOC removal efficiency (R<sub>TOC</sub>) for p-CR and p-TBP was calculated by the following equation (2):

$$R_{TOC} = (c_{o, TOC} - c_{e, TOC}) / c_{o, TOC} \times 100\% \quad (2)$$

## 3. Results and discussion

### 3.1. Comparative strategy of fabricating graphene oxide/manganese oxide composites

As shown in Fig. 1a and b, compared with *ex-situ* fabrication of GO/MnO<sub>2</sub> composites (Fig. 1b), a sustainable strategy of synchronously utilizing manganese ions and highly acidic wastewater was proposed to synthesize GO/MnO<sub>x</sub> composites (Fig. 1a). During *in-situ* synthesis of GO/MnO<sub>x</sub> composites (Fig. 1a), pristine GO/MnSO<sub>4</sub> suspension was produced using graphite, KMnO<sub>4</sub>, and H<sub>2</sub>SO<sub>4</sub> as ingredients. Then, the Mn<sup>2+</sup> was transformed into MnO<sub>x</sub> by adding additional KMnO<sub>4</sub> to obtain GO/MnO<sub>x</sub> composites. In addition, the mass flow analysis during synthesis of composites is shown in Fig. 1, indicating that *in-situ* synthesis exhibited better atom economy and less waste emission than *ex-situ* synthesis. Considering the

prospective production on a larger scale, GO/MnO<sub>x</sub> composites could be conveniently obtained via adding KMnO<sub>4</sub> into conventional synthesis process of GO. Especially, with increasing production demand of GO material, the *in-situ* synthesis provide a sustainable strategy for disposing acidic wastewater under the perspective of cleaner production. Specifically, the acidic wastewater containing abundant K<sup>+</sup>, SO<sub>4</sub><sup>2-</sup>, and H<sup>+</sup> could achieve sustainable utilization by concentration with evaporation or dialysis methods. In addition, desalinization treatment could be adopted to retain ion strength. The *in-situ* GO/MnO<sub>x</sub> composites could be continually produced by adding graphite and KMnO<sub>4</sub>, avoiding consuming a vast amount of H<sub>2</sub>SO<sub>4</sub> and discharging a mass of highly acidic wastewater in prospective application.

### 3.2. Characterization

The morphologies and heterostructure of samples are characterized by FE-SEM, TEM, and HRTEM (Fig. 2, Figure S1). GO exhibits a typical laminar structure, and presents some folding and wrinkles (Figure S1a). As shown in Figure S1b, tightly packed MnO<sub>2</sub> sheets could be assigned to layered δ-MnO<sub>2</sub>, which is in accordance with conventional preparation methods (Ren et al., 2011). It should be noted that the morphologies of manganese oxides in GO/MnO<sub>x</sub> (Fig. 2a and c) and GO/MnO<sub>2</sub> (Fig. 2b and d) composites are

distinctly different. Compared with mesoporous composites (Abbas et al., 2018; Awual et al. 2015a, 2017) and GO/MnO<sub>2</sub>, the HRTEM images of MnO<sub>x</sub> in GO/MnO<sub>x</sub> (Fig. 2e and f) show different crystal lattice in different regions. The isolated MnO<sub>x</sub> in GO/MnO<sub>x</sub> (Fig. 2e) presents ribbon-like structure with uniform crystal lattice. For MnO<sub>x</sub> stacked in GO/MnO<sub>x</sub> (Fig. 2f), anisotropic lattice fringes are observed, indicating the presence of mixed phase. In contrast, layered δ-MnO<sub>2</sub> is observed on the GO sheets for GO/MnO<sub>2</sub> composites (Fig. 2b and d). Moreover, EDX analysis of GO/MnO<sub>x</sub> and GO/MnO<sub>2</sub> composites (Figure S1c) reveals a nearly equivalent mass percentage of C, O, and Mn.

The N<sub>2</sub> adsorption-desorption isotherms, surface area, and pore distribution of samples are characterized as shown in Fig. 3. The N<sub>2</sub> isotherms of GO/MnO<sub>x</sub> (Fig. 3a) and GO/MnO<sub>2</sub> (Fig. 3b) composites exhibit type IV isotherm with an H3-type hysteresis loop according to IUPAC nomenclature, indicating presence of slit-shaped pores. GO/MnO<sub>x</sub> composites possess larger surface area (259.65 m<sup>2</sup>/g) and pore volume (0.44 cm<sup>3</sup>/g) than GO/MnO<sub>2</sub> composites (S<sub>BET</sub> = 92.08 m<sup>2</sup>/g, V<sub>p</sub> = 0.11 cm<sup>3</sup>/g). In addition, the sharp peak is observed in pore distribution of GO/MnO<sub>x</sub> composites due to uniform pore structure. Thus, the excellent pore structure and surface features provide GO/MnO<sub>x</sub> composites with better adsorption and removal performance than GO/MnO<sub>2</sub> composites.

To further illustrate crystal feature and structural differences of

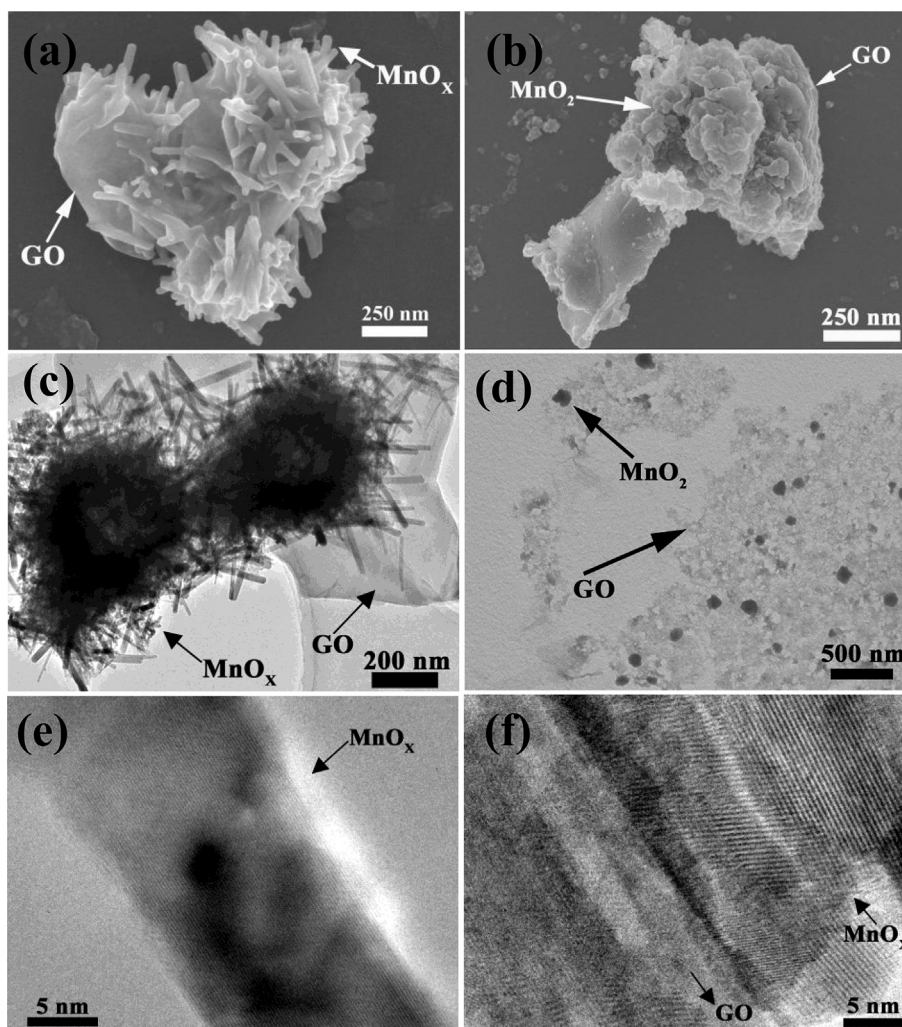


Fig. 2. FE-SEM images, TEM images, and HRTEM images of GO/MnO<sub>x</sub> (a, c, e, f) and GO/MnO<sub>2</sub> (b, d).

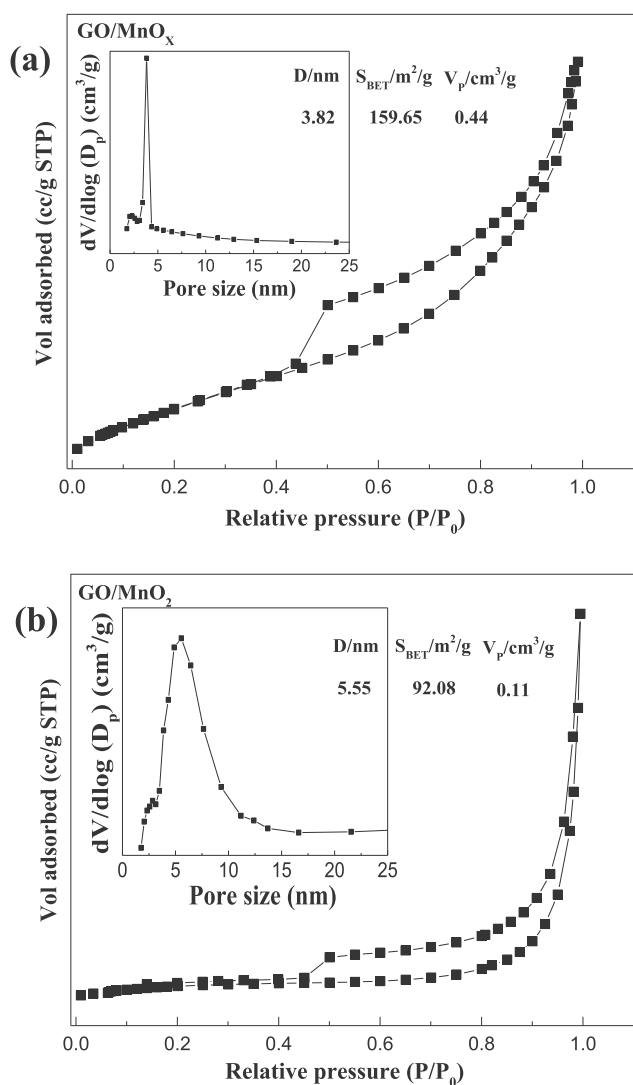


Fig. 3. N<sub>2</sub> adsorption-desorption isotherms and pore distribution (inset) of GO/MnO<sub>x</sub> (a) and GO/MnO<sub>2</sub> (b).

samples, XRD spectra of GO, MnO<sub>2</sub>, GO/MnO<sub>2</sub>, and GO/MnO<sub>x</sub> composites are performed. As shown in Figure S2, the diffraction peak at  $2\theta = 11.30^\circ$ , which is assigned to the (001) crystal plane of GO (Zhang et al. 2015, 2018b), disappears in the GO/MnO<sub>x</sub> and GO/MnO<sub>2</sub> composites. For pristine MnO<sub>2</sub>, the diffraction peaks at  $2\theta = 12.32^\circ$ ,  $37.44^\circ$ ,  $43.12^\circ$ , and  $66.56^\circ$  can be assigned to (003), (012), (015), and (110) crystal planes of  $\delta$ -MnO<sub>2</sub>, respectively (JCPDS 86–0666) (Luo et al., 2018; Meng et al., 2014). After combination with GO, the manganese oxides in GO/MnO<sub>2</sub> composites exhibit similar diffraction peaks with pristine MnO<sub>2</sub>. Unlike MnO<sub>2</sub> and GO/MnO<sub>2</sub> composites, the diffraction peaks of MnO<sub>x</sub> in GO/MnO<sub>x</sub> composites may match the mixed phase ( $X = 2, 3/4$ ) of  $\alpha$ -MnO<sub>2</sub> (JCPDS 44–0141) and Mn<sub>3</sub>O<sub>4</sub> (JCPDS 24–0734). Specifically, the diffraction peaks at  $2\theta$  of  $11.84^\circ$ ,  $24.64^\circ$ ,  $50.40^\circ$ , and  $60.00^\circ$  could be indexed to the (110), (310), (411), and (521) planes of  $\alpha$ -MnO<sub>2</sub>, respectively (Al-Sagheer and Zaki, 2000; Wang and Li, 2002; Xu et al., 2015a), and the diffraction peaks at  $2\theta$  of  $18.00^\circ$ ,  $32.64^\circ$ , and  $35.92^\circ$  could be attributed to the (101), (103), and (211) planes of Mn<sub>3</sub>O<sub>4</sub>, respectively (Jiangying et al., 2013).

FT-IR spectra are further performed to comparatively examine the functional groups transformation of GO/MnO<sub>x</sub> and GO/MnO<sub>2</sub> composites before and after combination. As shown in Figure S3,

the spectra of GO exhibit bands at  $3422$ ,  $1718$ ,  $1621$ , and  $1052\text{ cm}^{-1}$  corresponding to the stretching vibration of  $-\text{OH}$ ,  $\text{C}=\text{O}$ ,  $\text{C}=\text{C}$ , and  $\text{C}-\text{OH}$ , respectively (Xu et al., 2015b; Zhang et al., 2018b). The vibrational bands at  $1224$  and  $838\text{ cm}^{-1}$ , which are attributed to the anti-symmetric and symmetric stretching vibrations of  $\text{C}-\text{O}-\text{C}$  (Zhang et al., 2018a), disappear in the spectra of GO/MnO<sub>x</sub> composites. Meanwhile, a strong band at  $1130\text{ cm}^{-1}$  for GO/MnO<sub>x</sub> composites is assigned to the formation of covalent bonds ( $\text{Mn}-\text{O}-\text{C}$ ) (Xu et al., 2015b). The bands at about  $1400\text{ cm}^{-1}$  are ascribed to the in-plane bending vibration of the  $\text{C}-\text{O}-\text{H}$ , which is attributed to the retention of  $\text{C}-\text{O}-\text{H}$  after combination of GO and manganese oxides. For GO/MnO<sub>2</sub> composites, the strength of bands for oxygen-containing functional groups on GO sheets decreases with the combination of MnO<sub>2</sub>. Compared with GO/MnO<sub>x</sub> composites, the weaker  $\text{Mn}-\text{O}-\text{C}$  bonds are also observed on GO/MnO<sub>2</sub> composites. Moreover, the band of MnO<sub>2</sub> at  $544\text{ cm}^{-1}$  corresponding to the Mn-O bending vibration is red-shifted in the spectra of GO/MnO<sub>x</sub> composites ( $526\text{ cm}^{-1}$ ) and GO/MnO<sub>2</sub> composites ( $523\text{ cm}^{-1}$ ). The change of Mn-O bending vibration was related to the structural composition of manganese oxides (Rathour and Bhattacharya, 2018; Yang et al., 2005). And  $\alpha$ -MnO<sub>2</sub>,  $\delta$ -MnO<sub>2</sub>, and Mn<sub>3</sub>O<sub>4</sub> possessed different Mn-O bending vibration in FT-IR spectra. In addition, the formation of covalent bonds ( $\text{Mn}-\text{O}-\text{C}$ ) in GO/MnO<sub>x</sub> and GO/MnO<sub>2</sub> composites would influence the Mn-O bending vibration.

To further investigate the chemical component and features of samples, XPS spectra are recorded in Figure S4 and Fig. 4. As shown in Figure S4, the wide scan XPS spectra of samples exhibit raw peaks of characteristic elements (C, O, and Mn). In the high-resolution XPS Mn 3s spectra (Fig. 4a) of MnO<sub>2</sub>, GO/MnO<sub>x</sub>, and GO-MnO<sub>2</sub> composites, the energy separation between the two split peaks reflects the mean manganese valence (Lei et al., 2012; Toupin et al., 2004). Compared with the energy separation value  $\Delta\text{B.E.}$  of MnO<sub>2</sub> ( $\Delta\text{B.E.} = 4.70\text{ eV}$ ) and GO-MnO<sub>2</sub> ( $\Delta\text{B.E.} = 4.95\text{ eV}$ ), the higher  $\Delta\text{B.E.}$  of GO/MnO<sub>x</sub> ( $\Delta\text{B.E.} = 6.10\text{ eV}$ ) implies a lower manganese valence ( $\text{Mn(IV)} \rightarrow \text{Mn(III)} \rightarrow \text{Mn(II)}$ ), which is ascribed to the fact that more electrons exist in the 3d orbit. The Mn 2p spectra (Fig. 4b) of MnO<sub>2</sub> and GO-MnO<sub>2</sub> retain the same trend, confirming that Mn(IV) is dominant in both of them. In contrast, the chemical shift of Mn 2p<sub>3/2</sub> on GO/MnO<sub>x</sub> composites indicates obvious transformation of chemical environment for Mn atom, which is in accordance with the result of Mn 3s spectra. Furthermore, the raw peaks of Mn 2p<sub>3/2</sub> are deconvoluted into the fitting peaks at  $643.00\text{ eV}$  (Mn(IV)) and  $641.47\text{ eV}$  (Mn(II)), indicating coexistence of Mn(IV) and Mn(II) in GO/MnO<sub>x</sub> ( $X = 2, 3/4$ ) composites. The relevant dates are recorded in Table S2. As shown in Fig. 4c, the deconvolution of the O 1s peak of MnO<sub>2</sub> resolves to two fitting peaks at  $531.20\text{ eV}$  and  $530.00\text{ eV}$ , which are attributed to the Mn-OH and Mn-O-Mn. It should be noted that the O 1s spectra of GO/MnO<sub>x</sub> and GO-MnO<sub>2</sub> composites obviously change due to the involvement of GO sheets. According to the fitting peaks (Fig. 4c) and relevant date (Table S2) of samples, the Mn-O-C in GO/MnO<sub>x</sub> becomes the dominant component (41.1%) with a sharp decline of Mn-O-Mn, indicating the mass generation of covalent bonds when *in-situ* bonding with GO sheets. However, a relatively small proportion of Mn-O-C (7.39%) exists in GO-MnO<sub>2</sub> composites, suggesting that physical interaction may play a dominant role in the combination of GO and MnO<sub>2</sub> for the *ex-situ* method. In addition, for GO/MnO<sub>x</sub> and GO-MnO<sub>2</sub> composites, the content of  $\text{C}-\text{C}/\text{C}=\text{C}$  in C 1s spectra (Fig. 4d), representing the content of  $\text{sp}^2$ -hybridized domains, is higher than pristine GO. Meanwhile, the relative content of  $\text{C}-\text{O}$ ,  $\text{C}=\text{O}$ , and  $\text{O}-\text{C}=\text{O}$  decreases after combination. The results indicate that partly oxygen-containing functional groups are broken and reduced after introducing Mn atoms.

Based on the above characterization, the formation mechanism and structural properties of GO/MnO<sub>x</sub> and GO/MnO<sub>2</sub> composites

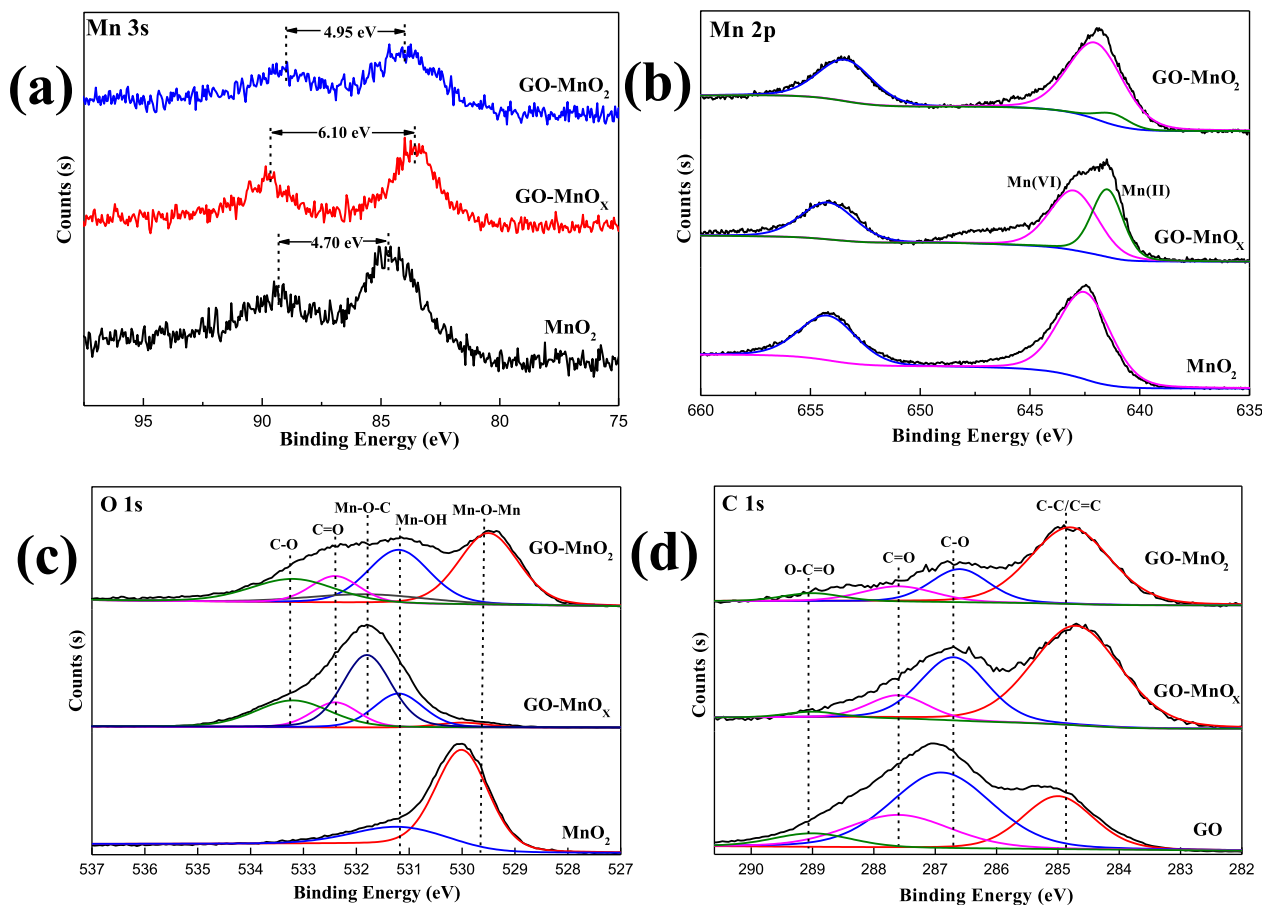


Fig. 4. XPS spectra of  $\text{MnO}_2$ ,  $\text{GO/MnO}_x$ , and  $\text{GO-MnO}_2$ : Mn 3s spectra (a), Mn 2p spectra (b), O 1s spectra (c); C 1s spectra (d) of GO,  $\text{GO/MnO}_x$ , and  $\text{GO-MnO}_2$ .

are further clarified. During the *in-situ* synthesis process of  $\text{GO/MnO}_x$  composites, the oxygen-containing functional groups (largely C-O-C and partly C=O) of GO sheets combine the Mn atoms by covalent Mn-O-C. Meanwhile, the mass of  $\text{Mn}_3\text{O}_4$  crystals is anchored onto the GO sheets via heterogeneous nucleation. Under the strong acid condition with  $\text{K}^+$  and  $\text{SO}_4^{2-}$ , partly  $\alpha\text{-MnO}_2$  nanowires generate and tightly grow on the GO sheets. Comparatively, during the *ex-situ* synthesis process of  $\text{GO/MnO}_2$  composites, layered  $\delta\text{-MnO}_2$  is stacked on the GO sheets via weak covalent bonds and physical interaction. In comparison with  $\text{GO-MnO}_2$  composites, the abundant Mn-O-C bonds (Toupin et al., 2004) in  $\text{GO/MnO}_x$  could provide an efficient channel for electron transfer from GO to  $\text{MnO}_x$ , thereby enhancing valence variation of Mn and the oxidation capacity for pollutants.

### 3.3. Adsorption and oxidation of p-CR and p-TBP

The adsorption and oxidation characteristics of  $\text{GO/MnO}_x$  and  $\text{GO/MnO}_2$  composites for the removal of p-CR and p-TBP are investigated by batch experiment. As shown in Fig. 5a, the removal efficiency and TOC removal efficiency of GO,  $\text{MnO}_2$ ,  $\text{GO/MnO}_x$ , and  $\text{GO/MnO}_2$  composites for p-CR and p-TBP are determined. GO presents the lowest removal efficiency for both p-CR and p-TBP. Although residual  $\text{sp}^2$ -hybridized domains possess  $\pi\text{-}\pi$  interaction with pollutants, the electrostatic repulsion between abundant oxygen functional groups on GO sheets and phenolic hydroxyl groups of pollutants impedes further adsorption of pollutants. In addition, pollutants-adsorbed GO sheets are dispersion-stable and difficult

to separate from aqueous solution due to their strong hydrophilicity with small size, leading to an unsatisfactory removal effect. Pristine  $\text{MnO}_2$  also exhibits good oxidation removal efficiency for pollutants. However, it should be noted that the relatively low TOC removal efficiency of  $\text{MnO}_2$  is probably due to the release of oxidation product (phenolic multimer and benzoquinones). After *in-situ* combining GO sheets and  $\text{MnO}_x$ , the  $\text{GO/MnO}_x$  composites exhibit the best removal efficiency and TOC removal efficiency for both p-CR and p-TBP. However, the *ex-situ*  $\text{GO/MnO}_2$  composites possess low removal capacity. The removal mechanism of  $\text{GO/MnO}_x$  and  $\text{GO/MnO}_2$  composites would be further elucidated with the following experiment investigation.

In addition, all samples present better removal efficiency and TOC removal efficiency for p-TBP than p-CR. This is because p-TBP, with low  $C_s$  and high  $K_{OW}$  (Table S1), possesses strong hydrophobic interaction with samples, and thus easily achieves adsorption separation from aqueous solution. Moreover, due to the existence of tertiary butyl as a strong electron-donating group, p-TBP is more likely to be oxidized than p-CR by manganese oxide in samples.

The initial pH is a key factor of influencing adsorption and oxidation capacity of samples. As shown in Figure S5, the removal efficiency for pollutants and variation tendency of dissolved Mn with different initial pH are determined to test removal properties and chemical stability of samples. For both  $\text{GO/MnO}_x$  and  $\text{GO/MnO}_2$  composites, the removal efficiency of p-CR (Figure S5a) and p-TBP (Figure S5b) exhibits high values at  $\text{pH} < 6$ , and gradually decreases with increasing initial pH. Under the acid condition, manganese oxides in samples possess stronger oxidation potential than under

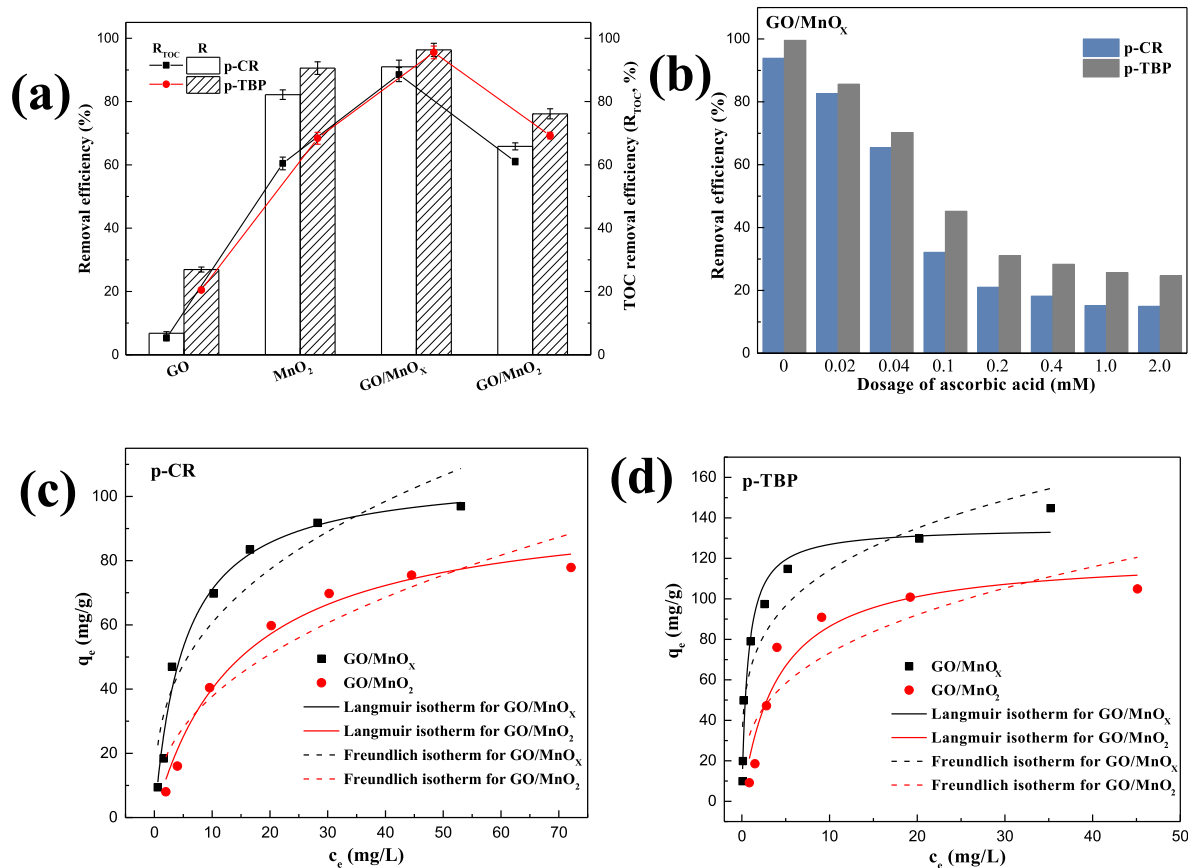


**Fig. 5.** Comparison of the removal efficiency and TOC removal efficiency of GO, MnO<sub>2</sub>, GO/MnO<sub>x</sub>, and GO/MnO<sub>2</sub> composites for p-CR and p-TBP (a); Effect of dosage of ascorbic acid as quenching agent on removal efficiency of p-CR and p-TBP by GO/MnO<sub>x</sub> composites (b); Langmuir and Freundlich isotherm parameters for the removal of p-CR (c) and p-TBP (d) by GO/MnO<sub>x</sub> and GO/MnO<sub>2</sub> composites at 25 °C. Experimental conditions: initial pH = 5, initial concentration = 50 mg/L, dosage = 1.0 g/L, contact time = 48 h, and T = 25 °C.

the alkaline condition (Zhang et al., 2009), thereby achieving higher oxidation removal capacity for pollutants. Moreover, according to Figure S6, the absolute value of zeta potentials for all samples in the acid condition is lower compared with the alkaline condition due to the protonation effect. Thus, partly reduced GO sheets both in GO/MnO<sub>x</sub> and GO/MnO<sub>2</sub> composites could ensure the effective adsorption of p-CR and p-TBP in the acid condition due to the weakened electrostatic repulsion and strong  $\pi$ - $\pi$  interaction. Thus, the changes of oxidation ability of samples and interaction (electrostatic and  $\pi$ - $\pi$  interaction) with pollutants cause the trend in pH analysis. Compared with GO/MnO<sub>2</sub> composites, GO/MnO<sub>x</sub> composites still exhibit high removal efficiency in the alkaline condition. Considering the removal efficiency and practical wastewater, pH 5.0 was chosen as the optimum pH in experiments.

In addition, it should be noted that the content of dissolved Mn for GO/MnO<sub>x</sub> composites is obviously lower than GO/MnO<sub>2</sub> composites at pH < 5. The Mn(II) cations could be reserved and involved into the re-oxidation process in GO/MnO<sub>x</sub> (Duan et al., 2016), leading to stronger affinity for Mn(II) than GO/MnO<sub>2</sub>. Especially for GO/MnO<sub>x</sub> composites, the strong acid condition during the synthetic process and Mn-O-C bonds ensure good structural stability at low pH. Thus, compared with GO/MnO<sub>2</sub> composites, GO/MnO<sub>x</sub> composites possess high removal efficiency and low content of dissolved Mn in a wider pH range for both p-CR and p-TBP.

The quenching experiment was carried out as shown in Fig. 5b and Figure S6b. The removal efficiency obviously declined with the increased ascorbic acid, indicating that oxidation process of p-CR and p-TBP by GO/MnO<sub>x</sub> composites was suppressed with interrupted electron transfer process. In addition, the removal efficiency

of GO/MnO<sub>2</sub> composites (Figure S6b) presented similar trend with addition of ascorbic acid. It should be noted that GO/MnO<sub>x</sub> and GO/MnO<sub>2</sub> composites still possessing a certain amount of removal capacities, which is ascribed to the adsorption of p-CR and p-TBP onto GO sheets in composites.

To further optimize experimental parameters and examine the difference of removal process between p-CR and p-TBP by GO/MnO<sub>x</sub> and GO/MnO<sub>2</sub> composites, the effect of contact time and temperature is determined by batch experiment. As shown in Figure S7, for both GO/MnO<sub>x</sub> and GO/MnO<sub>2</sub> composites, the removal of p-CR reaches equilibrium (approximately 8 h for GO/MnO<sub>x</sub> and 18 h for GO/MnO<sub>2</sub>) faster than p-TBP (approximately 24 h for GO/MnO<sub>x</sub> and 48 h for GO/MnO<sub>2</sub>), respectively. Compared with GO/MnO<sub>2</sub> composites, GO/MnO<sub>x</sub> composites exhibit more rapid equilibrium and higher removal efficiency for both p-CR and p-TBP, ensuring more effective application. In addition, with temperature rising, the removal efficiency for both p-CR and p-TBP by samples gradually decreases, indicating the exothermic nature of the removal process. To achieve well removal efficiency for p-CR and p-TBP and cost-optimal parameters, the contact time and temperature were set as 48 h and 25 °C. In addition, Langmuir and Freundlich isotherms are analyzed with removal capacities of GO/MnO<sub>x</sub> and GO/MnO<sub>2</sub> composites. As shown in Fig. 5 c, d, and Table S3, the results show that Langmuir isotherm possesses better fitting with higher value of R<sup>2</sup> than Freundlich isotherm, indicating that the adsorption of p-CR and p-TBP on composites tend to monolayer adsorption process. GO/MnO<sub>x</sub> composites exhibit higher maximum removal capacities for p-CR (107.68 mg/g) and p-TBP (135.41 mg/g) than GO/MnO<sub>2</sub> composites (98.64 mg/g for p-CR

and 121.86 mg/g for p-TBP).

The regeneration capabilities of GO/MnO<sub>x</sub> and GO/MnO<sub>2</sub> composites are further evaluated for practical application. As shown in Figure S8, the removal efficiency of samples for pollutants gradually decreases with increasing recycle number. The main reason for this is that the oxidation capacity of GO/MnO<sub>x</sub> and GO/MnO<sub>2</sub> composites for pollutants gradually weakens due to the reduction of Mn(IV) after recycling. Meanwhile, the content of dissolved Mn gradually decreases. For both GO/MnO<sub>x</sub> and GO/MnO<sub>2</sub> composites, the content of dissolved Mn for p-TBP is higher than p-CR due to stronger oxidation. It is also noteworthy that GO/MnO<sub>x</sub> composites could retain high removal efficiency for p-TBP (>90%) after five recycles, which is ascribed to strong adsorption and remaining oxidation capacity. In addition, GO/MnO<sub>x</sub> composites possess

higher removal efficiency after recycling and better regeneration than GO/MnO<sub>2</sub> composites, indicating the potential as a cost-effective material.

To further investigate the transformation of p-CR and p-TBP after adsorption and oxidation process for GO/MnO<sub>x</sub> and GO/MnO<sub>2</sub> composites, the products are detected by HPLC/MS-MS. The mass spectra at different retention times for p-CR and p-TBP are recorded in Figure S9 (GO/MnO<sub>x</sub>) and Figure S10 (GO/MnO<sub>2</sub>). The mass fragments of transformation products for p-CR and p-TBP at different retention times are also listed in Table S4 (GO/MnO<sub>x</sub>) and Table S5 (GO/MnO<sub>2</sub>). Accordingly, the tentative pathways of p-CR and p-TBP, comparing GO/MnO<sub>x</sub> and GO/MnO<sub>2</sub> composites, are shown in Fig. 6.

As shown in Fig. 6, Figure S9 and Table S4 (GO/MnO<sub>x</sub>), for p-CR,

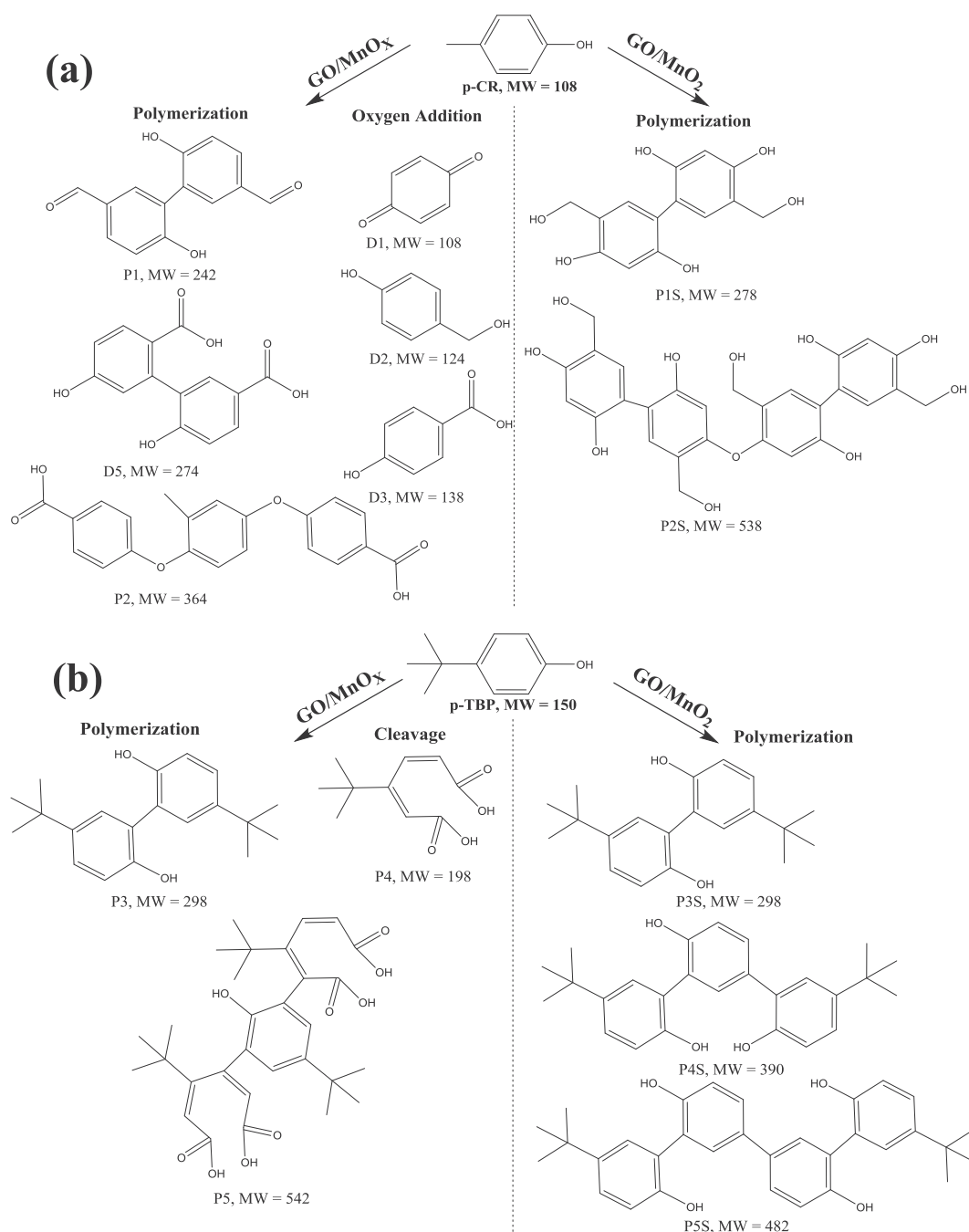


Fig. 6. Transformation products of p-CR (a) and p-TBP (b) by GO/MnO<sub>x</sub> and GO/MnO<sub>2</sub> composites.

the parent ion  $m/z$  241 at retention time 3.361 min may be assigned to the dimers (P1) of oxidation products via dimerization (Lu and Gan, 2013). Correspondingly, the possible structure of daughter ions reveals that the methyl in p-CR may be oxidized to form carbonyl (D1), hydroxyl (D2), and carboxyl (D3) via the oxygen addition process (Li et al., 2015). At retention time 13.264 min, the trimer (P2) of oxidation products for p-CR may be achieved, which is in accordance with the analysis of its daughter ions (D4 and D5). Regarding p-TBP, it should be noted that the parent ion  $m/z$  197 at retention time 9.592 min may be ascribed to the ring cleavage products (P4) of p-TBP, indicating that further oxidation occurs compared with p-CR.

Comparatively, as shown in Fig. 6, Figure S10 and Table S5, the oxidation products of p-CR and p-TBP by GO/MnO<sub>2</sub> composites are mainly assigned to the dimers (P1S for p-CR, and P3S for p-TBP), trimers (P4S for p-TBP), and tetramer (P2S for p-CR and P5S for p-TBP). The result indicates that GO/MnO<sub>x</sub> composites possess higher oxidation capacity than GO/MnO<sub>2</sub> composites via more varied oxidative pathways, such as oxygen addition and ring-opening reactions.

#### 3.4. Relationship between structure and adsorption-oxidation mechanism

Based on the above analysis of characterization, batch experiment, and transformation pathways, the relationship between different structure and adsorption-oxidation properties for the removal of pollutants by GO/MnO<sub>x</sub> and GO/MnO<sub>2</sub> composites is further clarified.

Compared with *ex-situ* GO/MnO<sub>2</sub> composites, *in-situ* GO/MnO<sub>x</sub> composites possess stronger removal properties with a synergistic effect between adsorption and oxidation due to their unique structure features.

Specifically, the adsorption of pollutants on partly reduced GO sheets promotes the removal process and oxidation capacity of GO/MnO<sub>x</sub> composites by enhancing mass transfer and electron transfer process. For GO/MnO<sub>x</sub> composites, the partly reduced GO sheets exhibit an enhanced  $\pi$ - $\pi$  interaction with pollutants, thereby accelerating diffusion of pollutants into the boundary layer. Similarly, the oxidation products and Mn(II) can be effectively diffused away from MnO<sub>x</sub> and adsorbed onto GO sheets, promoting the oxidation process. Moreover, abundant  $\pi$  electrons on partly reduced GO sheets can be transferred into MnO<sub>x</sub> as an electron source through Mn-O-C bonds during interaction with pollutants and promote one electron-transfer reactions. In addition, during oxidation of pollutants by MnO<sub>x</sub> ( $X = 2, 3/4$ , mixture of  $\alpha$ -MnO<sub>2</sub> and Mn<sub>3</sub>O<sub>4</sub>), Mn(IV) species is reduced to Mn(II) with generating intermediate Mn(III). Especially, the oxygen functional groups on GO sheets can re-oxidize Mn(II) as the oxidants to form Mn(III), and then participate in the oxidation of pollutants.

The oxidation of pollutants by MnO<sub>x</sub> contributes to the positive shift of adsorption equilibrium and augments the adsorption capacity of GO sheets by strengthening the charge-transfer interaction for GO/MnO<sub>x</sub> composites. After adsorption on GO sheets in GO/MnO<sub>x</sub> composites, pollutants (p-CR and p-TBP) are transferred into the MnO<sub>x</sub> surface and oxidized, changing the adsorption equilibrium. Thus, more pollutants are adsorbed and oxidized. In addition, during the oxidation of pollutants through sequential one electron-transfer reactions, the charge density on GO sheets is changed and produces many regions of electron deficiency. This is conducive to strengthening charge-charge interaction with electron-rich pollutants, thus enhancing adsorption capacity. However, for GO/MnO<sub>2</sub> composites, the weakened bonds between GO and MnO<sub>2</sub> are difficult to promote interactions with pollutants and achieve this synergistic effect between adsorption and oxidation. Thus, GO/

MnO<sub>2</sub> composites possess lower removal efficiency and less oxidized products for pollutants than GO/MnO<sub>x</sub> composites.

Both GO/MnO<sub>x</sub> and GO/MnO<sub>2</sub> composites exhibit higher removal efficiency for p-TBP than p-CR. Based on the above analysis of contrastive batch experiment, in comparison with p-CR, p-TBP exhibits stronger adsorption (hydrophobic interaction and  $\pi$ - $\pi$  interaction) with samples. Tertiary butyl in p-TBP as a strong electron-donating group is also more likely to be oxidized by manganese oxides. Especially for GO/MnO<sub>x</sub> composites, the transformation products of p-TBP contain not only dimer and trimer of oxidation products, but also ring cleavage products. The further oxidation for p-TBP contributes to the mineralization of p-TBP.

#### 3.5. Application expectation and environmental implications

Considering the application in actual phenolic pollution treatment, GO/MnO<sub>x</sub> composites could be employed as powdered treatment agent, which is similar to commercial powdered activated carbon. Based on the batch experiments, GO/MnO<sub>x</sub> composites exhibited well removal efficiency for wide concentration range of aromatic pollutants. Thus, in react units of sewage treatment plants, GO/MnO<sub>x</sub> powder could be applied in pretreatment unit to removal refractory aromatic pollutants. Also, during the advanced treatment after traditional biological treatment, GO/MnO<sub>x</sub> powder possessed excellent removal efficiency for low-level aromatic pollutants. Moreover, for urgently polluted water due to leakage of phenolic pollutants, it is convenient to utilize GO/MnO<sub>x</sub> powder and adjust the dosage along with the concentration of pollutants. In addition, mild reaction process in the system has the advantage of low requirements for devices and is easy to realize. In consideration of environmental implications, manganese oxides exhibited well feasibility as traditional oxidants in wastewater treatment. Although the introduction of GO-based materials into water environment remain research stage due to potential toxicological effects for organism, the effective separation and regeneration in batch experiments could promote progress in prospective application.

## 4. Conclusions

In summary, graphene oxide/manganese oxide (GO/MnO<sub>x</sub>, GO/MnO<sub>2</sub>) composites, synthesized via *in-situ* and *ex-situ* methods, possess different structural features and removal properties for p-CR and p-TBP. Compared with *ex-situ* GO/MnO<sub>2</sub> composites, *in-situ* GO/MnO<sub>x</sub> composites possess higher removal efficiency and TOC removal efficiency, lower content of dissolved manganese ions, and wider pH range for p-CR and p-TBP. The partly reduced GO sheets and MnO<sub>x</sub> ( $X = 2, 3/4$ ), combined with Mn-O-C covalent bonds in GO/MnO<sub>x</sub> composites, produce a synergistic effect of adsorption and oxidation during the removal process. Meanwhile, GO/MnO<sub>x</sub> composites exhibit stronger oxidation capacity for pollutants than GO/MnO<sub>2</sub> composites. Especially, cleavage of aromatic rings for p-TBP occurs during the further oxidation process by GO/MnO<sub>x</sub> composites, indicating the potential of mineralization for pollutants. Thus, by comparing structural features with different fabrication strategies and clarifying removal mechanisms, the work is anticipated to promote practical application of graphene oxide/manganese oxide composites in removing phenolic compounds.

#### Declarations of interest

None.

## Acknowledgements

This work was supported by the National Natural Science Foundation of China (grant no. 21677087) and the National Science and Technology Major Project of China “Environmental Protection Technology Integration and Key Equipment for Tight Reservoir Development” (grant no. 2016ZX05040-005). The authors express appreciation to Jake Carpenter from UCLA for linguistic assistance.

## Appendix A. Supplementary data

Supplementary data to this article can be found online at <https://doi.org/10.1016/j.jclepro.2019.01.055>.

## References

- Abbas, K., Znad, H., Awual, M.R., 2018. A ligand anchored conjugate adsorbent for effective mercury(II) detection and removal from aqueous media. *Chem. Eng. J.* 334, 432–443.
- Abdullah, W.N.W., Bakar, W.A.W.A., Ali, R., Mokhtar, W.N.A.W., Omar, M.F., 2017. Catalytic oxidative desulfurization technology of supported ceria based catalyst: physicochemical and mechanistic studies. *J. Clean. Prod.* 162, 1455–1464.
- Al-Sagheer, F.A., Zaki, M.I., 2000. Surface properties of sol–gel synthesized  $\delta$ -MnO<sub>2</sub> as assessed by N<sub>2</sub> sorptometry, electron microscopy, and X-ray photoelectron spectroscopy. *Colloids Surf., A* 173 (1), 193–204.
- Awual, M.R., 2014. Investigation of potential conjugate adsorbent for efficient ultra-trace gold(III) detection and recovery. *J. Ind. Eng. Chem.* 20 (5), 3493–3501.
- Awual, M.R., 2016. Ring size dependent crown ether based mesoporous adsorbent for high cesium adsorption from wastewater. *Chem. Eng. J.* 303, 539–546.
- Awual, M.R., 2017. Novel nanocomposite materials for efficient and selective mercury ions capturing from wastewater. *Chem. Eng. J.* 307, 456–465.
- Awual, M.R., Alharthi, N.H., Okamoto, Y., Karim, M.R., Halim, M.E., Hasan, M.M., Rahman, M.M., Islam, M.M., Khaleque, M.A., Sheikh, M.C., 2017. Ligand field effect for Dysprosium(III) and Lutetium(III) adsorption and EXAFS coordination with novel composite nanomaterials. *Chem. Eng. J.* 320, 427–435.
- Awual, M.R., Hasan, M.M., Khaleque, M.A., 2015a. Efficient selenium(IV) detection and removal from water by tailor-made novel conjugate adsorbent. *Sens. Actuators, B* 209, 194–202.
- Awual, M.R., Khaleque, M.A., Ratna, Y., Znad, H., 2015b. Simultaneous ultra-trace palladium(II) detection and recovery from wastewater using new class meso-adsorbent. *J. Ind. Eng. Chem.* 21, 405–413.
- Awual, M.R., Khraisheh, M., Alharthi, N.H., Luqman, M., Islam, A., Rezaul Karim, M., Rahman, M.M., Khaleque, M.A., 2018. Efficient detection and adsorption of cadmium(II) ions using innovative nano-composite materials. *Chem. Eng. J.* 343, 118–127.
- Buke, W., Guobin, Z., Mengyu, Y., Tengfei, X., Pan, H., Liang, H., Xu, X., Liqiang, M., 2018. Graphene scroll-coated  $\alpha$ -MnO<sub>2</sub> nanowires as high-performance cathode materials for aqueous Zn-ion battery. *Small* 14 (13), 1703850.
- Chen, S., Zhu, J., Wu, X., Han, Q., Wang, X., 2010. Graphene oxide–MnO<sub>2</sub> nanocomposites for supercapacitors. *ACS Nano* 4 (5), 2822–2830.
- Danquah, M.K., Aruei, R.C., Wilson, L.D., 2018. Phenolic pollutant uptake properties of molecular templated polymers containing  $\beta$ -cyclodextrin. *J. Phys. Chem. B* 122 (17), 4748–4757.
- Deng, J., Wang, X., Duan, X., Liu, P., 2015. Facile preparation of MnO<sub>2</sub>/graphene nanocomposites with spent battery powder for electrochemical energy storage. *ACS Sustain. Chem. Eng.* 3 (7), 1330–1338.
- Duan, L., Wang, Z., Hou, Y., Wang, Z., Gao, G., Chen, W., Alvarez, P.J.J., 2016. The oxidation capacity of Mn<sub>3</sub>O<sub>4</sub> nanoparticles is significantly enhanced by anchoring them onto reduced graphene oxide to facilitate regeneration of surface-associated Mn(III). *Water Res.* 103, 101–108.
- Grebel, J.E., Charbonnet, J.A., Sedlak, D.L., 2016. Oxidation of organic contaminants by manganese oxide geomedia for passive urban stormwater treatment systems. *Water Res.* 88, 481–491.
- Hummers, W.S., Offeman, R.E., 1958. Preparation of graphitic oxide. *J. Am. Chem. Soc.* 80 (6), 1339–1339.
- Jiang, J., Gao, Y., Pang, S.-Y., Lu, X.-T., Zhou, Y., Ma, J., Wang, Q., 2015. Understanding the role of manganese dioxide in the oxidation of phenolic compounds by aqueous permanganate. *Environ. Sci. Technol.* 49 (1), 520–528.
- Jiangqing, Q., Feng, G., Quan, Z., Zhiyu, W., Han, H., Beibei, L., Wubo, W., Xuzhen, W., Jiesshan, Q., 2013. Highly atom-economic synthesis of graphene/Mn<sub>3</sub>O<sub>4</sub> hybrid composites for electrochemical supercapacitors. *Nanoscale* 5 (7), 2999–3005.
- Jin, Z., Wang, X., Sun, Y., Ai, Y., Wang, X., 2015. Adsorption of 4-n-nonylphenol and bisphenol-A on magnetic reduced graphene oxides: a combined experimental and theoretical studies. *Environ. Sci. Technol.* 49 (15), 9168–9175.
- Kalembkiewicz, J., Sitarz-Palczak, E., Zapała, L., 2008. A study of the chemical forms or species of manganese found in coal fly ash and soil. *Microchem. J.* 90 (1), 37–43.
- Lei, Z., Shi, F., Lu, L., 2012. Incorporation of MnO<sub>2</sub>-coated carbon nanotubes between graphene sheets as supercapacitor electrode. *ACS Appl. Mater. Interfaces* 4 (2), 1058–1064.
- Li, G., Lu, Y., Lu, C., Zhu, M., Zhai, C., Du, Y., Yang, P., 2015. Efficient catalytic ozonation of bisphenol-A over reduced graphene oxide modified sea urchin-like  $\alpha$ -MnO<sub>2</sub> architectures. *J. Hazard. Mater.* 294, 201–208.
- Lu, Z., Gan, J., 2013. Oxidation of nonylphenol and octylphenol by manganese dioxide: kinetics and pathways. *Environ. Pollut.* 180, 214–220.
- Luo, K., Zhao, S.-X., Wang, Y.-F., Zhao, S.-J., Zhang, X.-H., 2018. Synthesis of petal-like  $\delta$ -MnO<sub>2</sub> and its catalytic ozonation performance. *New J. Chem.* 42 (9), 6770–6777.
- Meng, Y., Song, W., Huang, H., Ren, Z., Chen, S.-Y., Suib, S.L., 2014. Structure–property relationship of bifunctional MnO<sub>2</sub> nanostructures: highly efficient, ultra-stable electrochemical water oxidation and oxygen reduction reaction catalysts identified in alkaline media. *J. Am. Chem. Soc.* 136 (32), 11452–11464.
- Ou, H., Zhang, W., Yang, X., Cheng, Q., Liao, G., Xia, H., Wang, D., 2018. One-pot synthesis of g-C<sub>3</sub>N<sub>4</sub>-doped amine-rich porous organic polymer for chlorophenol removal. *Environ. Sci.: Nano* 5 (1), 169–182.
- Qu, J., Shi, L., He, C., Gao, F., Li, B., Zhou, Q., Hu, H., Shao, G., Wang, X., Qiu, J., 2014. Highly efficient synthesis of graphene/MnO<sub>2</sub> hybrids and their application for ultrafast oxidative decomposition of methylene blue. *Carbon* 66, 485–492.
- Rathour, R.K.S., Bhattacharya, J., 2018. A green approach for single-pot synthesis of graphene oxide and its composite with Mn<sub>3</sub>O<sub>4</sub>. *Appl. Surf. Sci.* 437, 41–50.
- Remucal, C.K., Ginder-Vogel, M., 2014. A critical review of the reactivity of manganese oxides with organic contaminants. *Environ. Sci.: Processes Impacts* 16 (6), 1247–1266.
- Ren, Y., Yan, N., Wen, Q., Fan, Z., Wei, T., Zhang, M., Ma, J., 2011. Graphene/ $\delta$ -MnO<sub>2</sub> composite as adsorbent for the removal of nickel ions from wastewater. *Chem. Eng. J.* 175, 1–7.
- Toupin, M., Brousse, T., Bélanger, D., 2004. Charge storage mechanism of MnO<sub>2</sub> electrode used in aqueous electrochemical capacitor. *Chem. Mater.* 16 (16), 3184–3190.
- Villar da Gama, B.M., Elisandra do Nascimento, G., Silva Sales, D.C., Rodríguez-Díaz, J.M., Bezerra de Menezes Barbosa, C.M., Menezes Bezerra Duarte, M.M., 2018. Mono and binary component adsorption of phenol and cadmium using adsorbent derived from peanut shells. *J. Clean. Prod.* 201, 219–228.
- Wan, S., Ding, W., Wang, Y., Wu, J., Gu, Y., He, F., 2018. Manganese oxide nanoparticles impregnated graphene oxide aggregates for cadmium and copper remediation. *Chem. Eng. J.* 350, 1135–1143.
- Wang, J., Zhang, G., Zhang, P., 2018a. Graphene-assisted photothermal effect on promoting catalytic activity of layered MnO<sub>2</sub> for gaseous formaldehyde oxidation. *Appl. Catal., B* 239, 77–85.
- Wang, L., Jiang, J., Pang, S.-Y., Zhou, Y., Li, J., Sun, S., Gao, Y., Jiang, C., 2018b. Oxidation of bisphenol A by nonradical activation of peroxymonosulfate in the presence of amorphous manganese dioxide. *Chem. Eng. J.* 352, 1004–1013.
- Wang, X., Li, Y., 2002. Selected-control hydrothermal synthesis of  $\alpha$ - and  $\beta$ -MnO<sub>2</sub> single crystal nanowires. *J. Am. Chem. Soc.* 124 (12), 2880–2881.
- Wang, X., Qin, Y., Zhu, L., Tang, H., 2015. Nitrogen-doped reduced graphene oxide as a bifunctional material for removing bisphenols: synergistic effect between adsorption and catalysis. *Environ. Sci. Technol.* 49 (11), 6855–6864.
- Xu, H., Qu, Z., Zhao, S., Mei, J., Quan, F., Yan, N., 2015a. Different crystal-forms of one-dimensional MnO<sub>2</sub> nanomaterials for the catalytic oxidation and adsorption of elemental mercury. *J. Hazard. Mater.* 299, 86–93.
- Xu, H., Qu, Z., Zong, C., Huang, W., Quan, F., Yan, N., 2015b. MnOx/graphene for the catalytic oxidation and adsorption of elemental mercury. *Environ. Sci. Technol.* 49 (11), 6823–6830.
- Yan, H., Li, H., Tao, X., Li, K., Yang, H., Li, A., Xiao, S., Cheng, R., 2014. Rapid removal and separation of iron(II) and manganese(II) from micropolluted water using magnetic graphene oxide. *ACS Appl. Mater. Interfaces* 6 (12), 9871–9880.
- Yang, R., Wang, Z., Dai, L., Chen, L., 2005. Synthesis and characterization of single-crystalline nanorods of  $\alpha$ -MnO<sub>2</sub> and  $\gamma$ -MnOOH. *Mater. Chem. Phys.* 93 (1), 149–153.
- Ye, R., Dong, J., Wang, L., Mendoza-Cruz, R., Li, Y., An, P.-F., Yacamán, M.J., Yakobson, B.I., Chen, D., Tour, J.M., 2018. Manganese decoration on graphene and implications in catalysis. *Carbon* 132, 623–631.
- Zagklis, D.P., Paraskeva, C.A., 2015. Purification of grape marc phenolic compounds through solvent extraction, membrane filtration and resin adsorption/desorption. *Separ. Purif. Technol.* 156, 328–335.
- Zhang, B., Li, F., Wu, T., Sun, D., Li, Y., 2015. Adsorption of p-nitrophenol from aqueous solutions using nanographite oxide. *Colloids Surf., A* 464, 78–88.
- Zhang, B., Li, Y., Wu, T., Sun, D., Chen, W., Zhou, X., 2018a. Magnetic iron oxide/graphene oxide nanocomposites: formation and interaction mechanism for efficient removal of methylene blue and p-tert-butylphenol from aqueous solution. *Mater. Chem. Phys.* 205, 240–252.
- Zhang, H., Da, Z., Feng, Y., Wang, Y., Cai, L., Cui, H., 2018b. Enhancing the electricity generation and sludge reduction of sludge microbial fuel cell with graphene oxide and reduced graphene oxide. *J. Clean. Prod.* 186, 104–112.
- Zhang, L., Ma, J., Li, X., Wang, S., 2009. Enhanced removal of organics by permanganate preoxidation using tannic acid as a model compound – role of in situ formed manganese dioxide. *J. Environ. Sci.* 21 (7), 872–876.
- Zhong, W., Wang, D., Wang, Z., 2018. Distribution and potential ecological risk of 50 phenolic compounds in three rivers in Tianjin, China. *Environ. Pollut.* 235, 121–128.